International Journal of Heat and Mass Transfer 203 (2023) 123837

Contents lists available at ScienceDirect

International Journal of Heat and Mass Transfer

journal homepage: www.elsevier.com/locate/hmt

On critical heat flux and its evaporation momentum and hydrodynamic limits

Suhas Tamvada[a], Daniel Attinger[b], Saeed Moghaddam[a,*]

[a] Mechanical and Aerospace engineering, University of Florida, Gainesville, FL 32611, United States
[b] Struo LLC, Ames, IA 50010, United States

ARTICLE INFO

Article history:
Received 15 August 2022
Revised 23 December 2022
Accepted 30 December 2022
Available online 7 January 2023

Keywords:
Pool boiling
Critical heat flux
Hydrodynamic limit
Evaporation momentum limit

ABSTRACT

The upper limit of heat transfer from a heated surface to a surrounding boiling liquid has been the subject of numerous studies ever since Nukiyama (1934) discovered this limit. The underlying physics governing this phenomenon, universally known as the critical heat flux (CHF) limit, has been extensively debated for nearly a century. Two prevailing hypotheses have emerged including hydrodynamic instability and evaporation momentum force thresholds proposed by Kutateladze (1948) and Steinchen and Sefiane (1996), respectively. Zuber (1959) and Kandlikar (2001) developed correlations based on these hypotheses that predict roughly similar CHF values i.e., ~100 W/cm^2 for water at 1 atm on a copper surface. Here, we present experimental and analytical studies conducted on liquids with a wide range of thermophysical properties on planar heater surfaces of different size (to stabilize the flow hydrodynamics) that show the evaporation momentum limit (CHF_{EM}) is roughly 4 times the Zuber's limit (CHF_{Zuber}). We show that CHF_{EM} can only be observed when hydrodynamics of liquid and vapor above the surface is stabilized, delineating an ultimate limit governed by a force balance at the surface-fluid interface rather than the instability of liquid and vapor interface away from the surface. We find that CHF/CHF_{EM} varies from 0.2 to 1 for all fluids, saturation temperatures, and heater geometries tested, representing 48 conditions.

1. Introduction

Boiling heat transfer is a critical phenomenon in a broad range of industries such as power generation [1], thermal desalination [2,3], chemical processing [4], cooling/refrigeration [5], and thermal management of electronics and laser diodes [6]. Nucleate boiling can dissipate significantly higher heat fluxes relative to single-phase liquid convection [7]. One of the long-standing questions in this field of science concerns the underlaying physics of the upper limit of this heat transfer mode, commonly known as the critical heat flux (CHF). At CHF, an enveloping vapor blanket triggers a rapid, often catastrophic, rise in the heater temperature leading to heater burnout [7]. CHF is the chief thermal performance limiter in light water-cooled nuclear reactors [8]. Hence, insights into the underlying physics of CHF could engender enhancement strategies that may benefit energy production and use.

Since the identification of CHF in 1934 by Nukiyama [9], close to a century of research has revolved around understanding the physics of this phenomenon and increasing its limit. The effects of liquid properties [10–12], surface wettability [13–15], wickability [16–20], roughness [21–23], size [24,25], and orientation [24,26–30] have been studied. The most prominent explanation of CHF has been in the form of the hydrodynamic theory, initially conceived by Kutateladze [31] and later presented as a mathematical correlation by Zuber [32] in 1958. The hydrodynamic theory attributes CHF to instability of liquid and vapor columns above the heater surface. The hydrodynamic theory largely prevailed as the most plausible explanation of CHF for roughly 4 decades [33]. In 1982, Haramura and Katto [34] proposed the macrolayer dryout model postulating that a thin liquid layer surrounding a bubble supplies liquid to the surface and the dryout of this liquid layer causes CHF. In 1996, Steinchen and Sefiane [35] considered the possibility of the boiling crisis being triggered by rapid vapor recoil at the liquid-solid contact line giving rise to the evaporation momentum theory. Kandlikar incorporated the effects of liquid-surface contact angle and heater orientation to develop a correlation based on the evaporation momentum force theory [36].

Fig. 1(A, B) depict the underlying physics of these two prominent hypotheses. The hydrodynamic theory proposed by Zuber [32] postulates that as heat flux is increased, the rate of bubble nucleation increases, eventually leading to stable vapor columns (see Fig. 1(A)) which become steady pathways for departing vapor. As the velocity of vapor streams increases, they interfere with the

* Corresponding author.
E-mail address: saeedmog@ufl.edu (S. Moghaddam).

https://doi.org/10.1016/j.ijheatmasstransfer.2022.123837
0017-9310/

Nomenclature

h_{fg}	latent heat of vaporization
h	copper fin height
l	copper fin length
w	copper fin width
Δx	distance between two thermocouples
i	current
A	heater area
g	acceleration due to gravity
L_h	characteristic heater length
F	force acting on a vapor pocket
$\dot{m}$	mass flux of vapor
d	diameter
k	thermal conductivity
T	temperature
$q"$	heat flux
ΔT	temperature difference in two consecutive thermocouples
V	voltage
P	power
L_c	capillary length
$\Delta\rho$	difference in liquid and vapor densities
Bo	bond number
r	radius
v	velocity of vapor
β	contact angle of vapor pocket

Greek symbols

λ_D	critical distance between consecutive vapor columns
ρ	density
σ	surface/interfacial tension

Subscripts

Cu	copper
w	water
c	contact parameter
e	ethanol
f	perfluorohexane (FC-72)
sol	solder
s	surface
$PDMS$	polydimethylsiloxane
m	evaporation momentum
b	vapor pocket

returning liquid. Zuber hypothesized that CHF is triggered when the velocity of vapor columns reaches a critical value corresponding to a critical distance between the columns (λ_D) such that the vapor-liquid interface destabilizes, consistent with the Taylor [37] and Helmholtz [38] instability, restricting liquid return to the surface. In essence, the hydrodynamic theory hypothesizes that CHF is triggered by a hydrodynamic phenomenon away from the fluid-surface interface. The hydrodynamic theory has been extensively used to predict CHF, and several modifications have been made to account for the effect of contact angle, roughness, and surface wickability. [39]. However, empirical factors are often used to match the experimental data [40].

On the other hand, the evaporation momentum theory considers the force balance at the three-phase contact line on the heater surface. Considering a dry patch on the surface (see Fig. 1(B)), which could be the result of a vapor column or pocket, Steinchen and Sefiane [35] proposed that CHF is triggered due to the momentum generated by rapid evaporation of liquid (denoted by gray squiggly lines). The momentum generated thus exerts a net lateral force on the vapor-liquid interface (shown by the red arrows) pushing the liquid radially outward, expanding the vapor-heater contact area. This force is only countered by the restoring surface tension of the liquid and buoyancy of the vapor pocket [36]. According to the evaporation momentum force theory, CHF is triggered when the balance between these forces tilts in favor of the evaporation momentum force, leading to rapid outward expansion of the vapor pocket.

Although the physics considered under these two hypotheses are drastically different, they have thus far been interchangeably used to predict similar values for CHF ($\sim 10^6$ W/m^2 for water on a smooth copper surface at 1 atm), and neither is able to explain experimental results of CHF surpassing the proposed limits [41]. Here, we study the hydrodynamic and evaporation momentum force hypotheses, to determine which mechanism is responsible for CHF. To this end, we have devised a set of experiments and conducted a theoretical analysis which unambiguously show that the limits of these mechanisms are vastly difference and they cannot be limiting at the same conditions.

2. Materials and methods

2.1. Tested liquids

Three different liquids; namely water, ethanol, and n-perfluorohexane (3 M Fluorinert FC-72©) were chosen for their industrial relevance and widely different thermophysical properties. Table 1 shows pertinent properties of the liquids at 25 °C and 1 atm (101.325 kPa). Latent heats of vaporization given in Table 1 are at their respective saturation conditions at 1 atm.

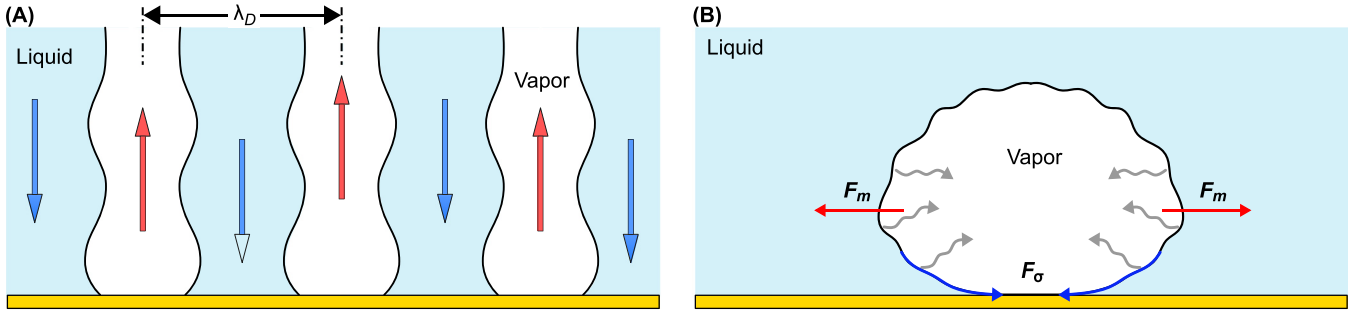

Fig. 1. Prevalent theories explaining CHF. (A) Hydrodynamic theory postulates that the interaction of escaping vapor (denoted by red arrows) and returning liquid (denoted by blue arrows) columns away from the surface trigger CHF when the distance between the vapor columns reaches a critical value (λ_D) based on Taylor instability [37]. (B) A vapor pocket growing on a hot surface is subject to a momentum force $\boldsymbol{F_m}$ (direction of force shown by red arrows), due to evaporating vapor (shown by squiggly gray arrows), which tries to expand the pocket radially outwards, and the surface tension force $\boldsymbol{F_\sigma}$ (shown by the blue arrows) acting along the periphery of the vapor pocket which work to retain the shape of the bubbles and pin the vapor pocket to the surface. Evaporation momentum theory states that CHF is triggered when the evaporation momentum force outweighs the restoring forces.

Table 1
Thermophysical properties of tested liquids at 25 °C and 1 atm (101.325 kPa). Latent heats of vaporization are at saturation conditions at 1 atm.

Liquid	Liquid density ρ_l (kg/m^3)	Vapor density ρ_v (kg/m^3)	Surface tension σ (N/m)	Latent heat of vaporization h_{fg} (kJ/kg)
Water	998	0.59	0.072	2256.4
Ethanol	789	1.59	0.022	918.16
FC-72	1680	13.13	0.010	88

2.2. Test device

The test article depicted in Fig. 2 consists of a copper furnace embedded in a Polytetrafluoroethylene (PTFE) block and houses two cartridge heaters of power 315 W each. Copper fins of height (h) 20 mm, length (l) 10 mm and widths (w) 10, 2, 1, and 0.5 mm were integrated into the furnace using a high-temperature solder ($Pb_{93.5}Sn_5Ag_{1.5}$, purchased from Digi-Key) to obtain 4 test surfaces. Four 'T' type thermocouples were soldered (k_{sol} = 60 W/m-K) into microposts machined on the side of the fin with the topmost thermocouple (T_1) placed 0.5 mm below the surface to measure temperature gradient along the fin height (see Fig. 2(A)).

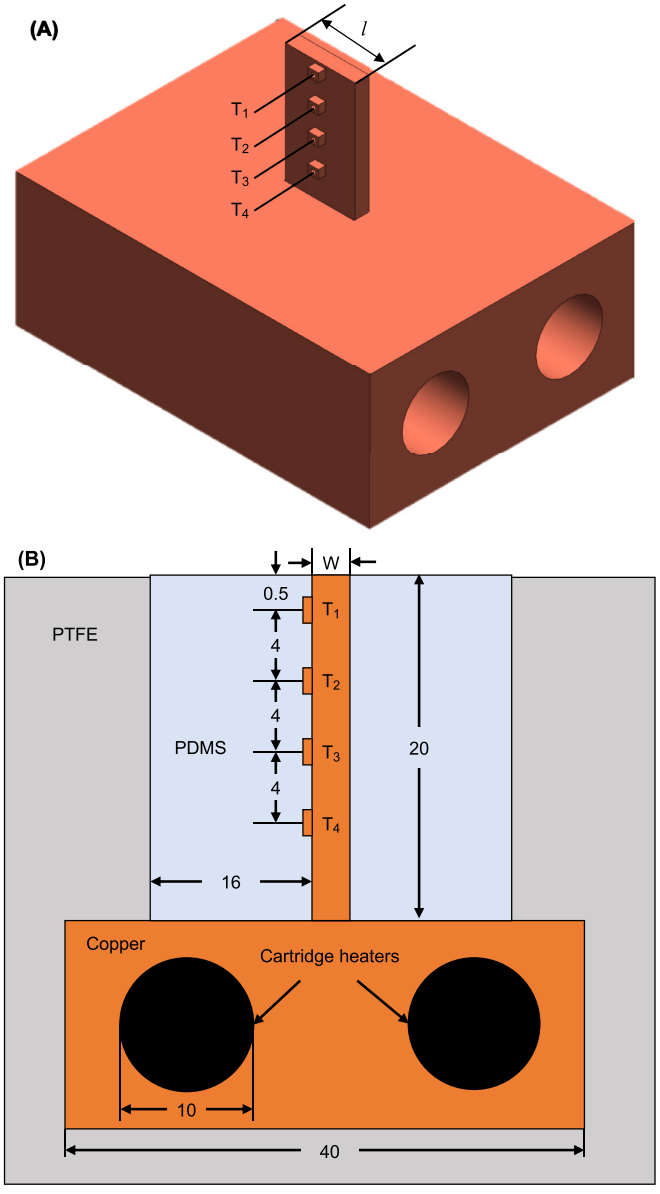

Fig. 2. Construction of test device. (A) A 3-D rendering of the copper component of the test apparatus shows placement of the 4 thermocouples on the longer side of the fin. (B) Cross section of the test device showing the furnace, copper fin, and the PDMS and PTFE insulation. The width (w) was altered to produce different test surfaces of 10, 2, 1, and 0.5-mm width. All dimensions are in mm.

The fins were insulated laterally using a 16 mm-thick layer of polydimethylsiloxane (PDMS) since the thermal conductivity of PDMS (k_{PMDS} = 0.15 W/m-K) is ~2500 times lower than that of copper (k_{Cu} = 398 W/m-K), resulting in negligible heat loss to surroundings (see Section 2.6). Heat flux between 2 consecutive thermocouples was measured using Fourier's law, $q" = -k_{Cu}(\Delta T/\Delta x)$, where ΔT is the temperature difference between the two thermocouples, and Δx (4 mm) is the spacing between them. Surface temperatures (T_s) were determined by extrapolating thermocouples measurements, and the reported heat flux is the average of 3 calculated heat fluxes.

2.3. Surface preparation

All surfaces were polished with sandpapers of 1500 grit, followed by 3000 grit. Next, they were polished using a metal polish (MAAS metal polish). Finally, they were washed, in order, with acetone, ethanol, isopropyl alcohol, and deionized water. Consistent liquid contact angles of 58 ± 2, 12 ± 2, and 4 ± 1 for water, ethanol, and FC-72, respectively, were recorded prior to experiments.

2.4. Experimental setup

A schematic of the experimental test setup is shown in Fig. 3. The test article was placed inside a vacuum chamber of external dimensions 8 × 8 × 8 in^3 (200 × 200 × 200 mm^3) with 4 quartz side walls for visualization. Light sources illuminated the test article, diffuser plates diffused the incident light, and power supplies powered the cartridge heaters through an electrical feedthrough (in red). Two auxiliary heaters of 500 W each were used to heat the working liquid to the test temperatures and consequently vary the pressure inside the chamber. A 5th T-type thermocouple immersed in the working liquid measured the saturation temperature (T_{sat}) of the liquid. By varying the supplied power to the auxiliary heaters, the saturation pressure and temperature (T_{sat}) were maintained constant. Details of pressure control are provided in the supplementary information (Section S1).

Two high-speed cameras (Photron FASTCAM SA4) were operated synchronously using the Photron FASTCAM PFV4 software in orthogonal directions for imaging close to the heater surface. High speed videos were recorded at a frame size of 856 × 856 pixels and 6000 fps resulting in a spatial and temporal resolution of 2 μm and 0.16 ms, respectively. A thermocouple feedthrough was used for recording temperature while a pressure transducer recorded the chamber pressure.

2.5. Experimental procedure

During an experiment, the test setup was first placed inside the chamberand the chamber was sealed using copper gaskets rated for high vacuum. Next, the liquid was degassed by vacuuming the chamber for 3 to 4 hours. This resulted in the "boiling" of the liquid at room temperature. It was verified that the saturation pressure of the liquid inside the chamber corresponded to the room temperature before experimental trials were started.

The pressure inside the chamber was adjusted using auxiliary heaters such that the temperature and pressure conditions inside the chamber followed the liquid saturation pressure curve. Next, AC power was supplied to the cartridge heaters in the furnace

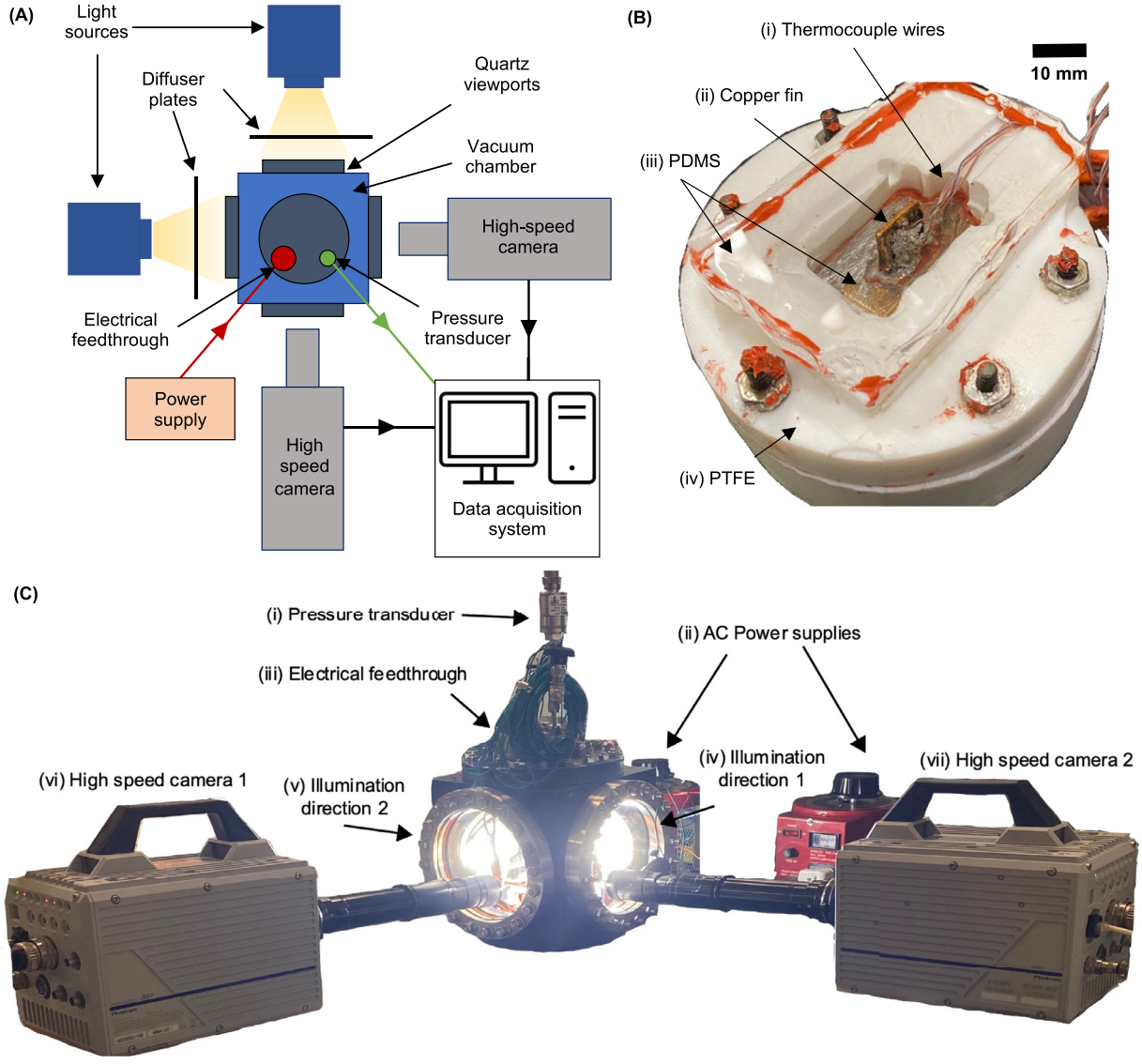

Fig. 3. Experimental test setup. (A) Schematic shows the experimental layout consisting of the light sources, vacuum chamber, high-speed cameras, power supply, Data Acquisition System (DAQ), and pressure transducer. The arrows show the direction of information transfer. **(B)** An image of the test device shows thermocouples (i) soldered into the fin, the copper fin (ii) brazed into the furnace, and the PDMS (iii) cast around the copper fin. The entire copper fixture is enclosed inside a PTFE (iv) block to insulate it from the surrounding liquid. **(C)** An image of the experimental setup from the side shows the (i) Pressure transducer, (ii) AC power supplies, (iii) Electrical feedthrough, (iv), (v) directions of illumination of the setup for recording high-speed movies, and (vi), (vii) the high-speed cameras used for recording synchronous videos of the boiling process.

in increments and increased after temperatures reached a steady state. During an experiment, an increase in heat flux is indicated by an increase in the difference between consecutive thermocouple readings (ΔT) as shown in Fig. 4., where T_1, T_2, T_3, and T_4 are thermocouple readings as described in Fig. 2. However, a drastic increase in all thermocouple readings as seen in Fig. 4 causes the difference between temperatures to become virtually zero (i.e., all thermocouples read the same temperature), indicating CHF. At this point, the experiment is stopped.

2.6. Heat loss from copper fin

Lateral heat loss from the copper fin can contribute to incorrect estimation of the heat flux. We quantified heat loss in the system by two methods – first, we measured the input voltage (V) and current (i) supplied to the cartridge heaters. This input power ($P = i$ x V) was compared with the power output, calculated by multiplying heat flux at the surface with the area ($q'' \times A$). The heat loss is found to be less than 5% in all our experimental trials. Secondly, we compare the three heat fluxes measured between the thermocouples with the average heat flux as shown in Fig. 5. Lateral heat loss in the fin implies a difference in the three heat fluxes; however, across all our experiments, these three heat fluxes deviate less than 2%. A theoretical analysis using a COMSOL model is also provided in the supplementary information (Section S3).

2.7. Data reduction

Temperature readings from boiling tests conducted at 4 different pressures (16.6, 33.3, 66.7, and 101.3 kPa) were reduced to heat fluxes as described in Section 2.2, and the maximum heat fluxes recorded at CHF, as described in Section 2.5, are reported. In addition, boiling curves (showing heat flux vs. surface superheat temperature) for experiments conducted at atmospheric pressure are plotted in supplementary information Section S2 alongside numerical simulations for natural convection at low

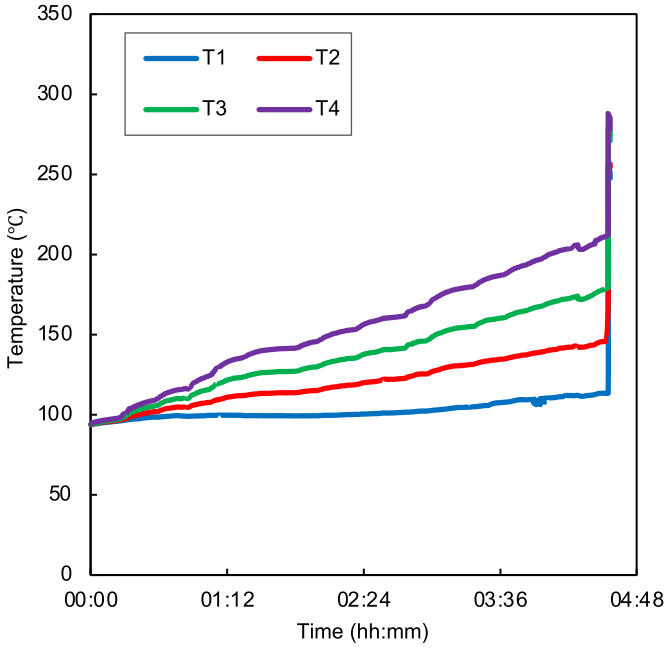

Fig. 4. Thermocouple readings during an experiment as a function of elapsed time (in hh:mm) show the determination of CHF limit during an experiment. The temperatures T_1, T_2, T_3, and T_4 represent thermocouple locations as described in Fig. 2. Towards the end of the experiment, temperatures sharply rise indicating CHF.

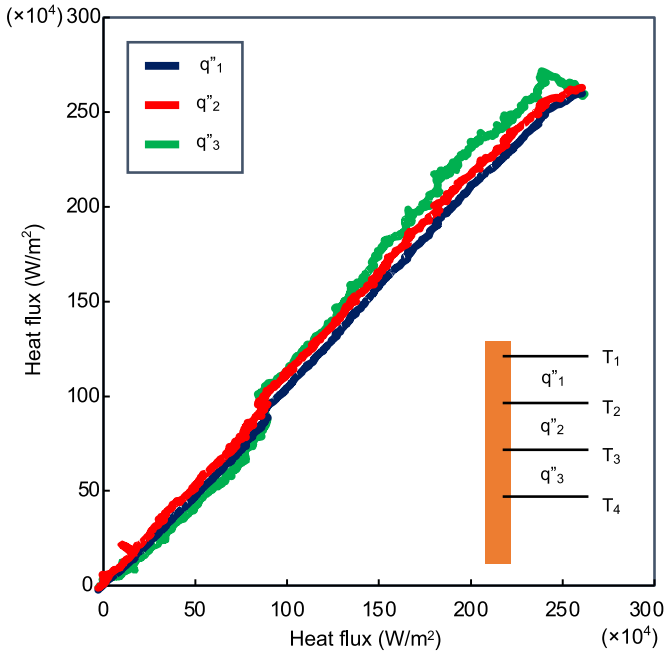

Fig. 5. Heat flux calculated at three different locations plotted as a function of average heat flux. No significant deviation in the heat flux at three different locations indicates that there is no heat loss across the fin section of the copper.

superheat temperatures. High-speed videos are analyzed using ImageJ, an open-source image processing software. The images are analyzed to characterize the progression of boiling and determine dynamic contact angles of the liquid near CHF.

2.8. Uncertainty and error analysis

The uncertainty in heat flux is caused by error in temperature readings, thermal conductivity of copper, and spacing between the thermocouples. Eq. (1) was used to calculate the uncertainty in heat flux

$$\frac{\delta q''}{q''} = \left[\left(\frac{\delta k}{k}\right)^2 + \left(\frac{\delta \Delta T}{\Delta T}\right)^2 + \left(\frac{\delta \Delta x}{\Delta x}\right)^2\right]^{(1/2)} \quad (1)$$

where δk, $\delta \Delta T$, $\delta \Delta x$ are the uncertainties in thermal conductivity, temperature gradient, and distance between thermocouples, respectively. Since the surface heat flux is the average of the three heat fluxes, the temperature difference is calculated as $\Delta T = (T_1 + T_2 + T_3 + T_4)/4$. Hence, $\delta \Delta T$ can be calculated using Eq. (2)

$$\delta \Delta T = \left[(\delta T)^2 + (\delta T)^2 + (\delta T)^2 + (\delta T)^2\right]^{(1/2)} \sim 2\delta T \quad (2)$$

The uncertainty in different experimental variables is tabulated in Table 2. The uncertainty in heat flux is found to be ±20.2% at a lower value of 14 $\times 10^4$ W/m^2 and ±3.1% at the highest value of 370 $\times 10^4$ W/m^2.

Table 2
Uncertainties of measured variables.

Variable	Uncertainty
δT	±0.65 K
$\delta k/k$	±2%
$\delta \Delta x/\Delta x$	±0.3%
$\delta A/A$	0.2%
$\delta P/P$	±0.25%

3. Results and discussion

3.1. Experimental observations

Fig. 6(A–C) show evolution of the boiling process leading up to CHF on different heaters. At the outset, it is prudent to note that we observe no significant difference in the mechanistic trends displayed by the three different liquids leading up to CHF (i.e., the visual analysis presented in Fig. 6(A–C) is representative of all tested liquids). However, to maintain consistency, all images shown in Fig. 6(A–C) are extracted from experiments conducted using ethanol at 101 kPa. Red dashed lines demarcate the heaters boundaries. Fig. 6(A) shows bubble behavior at different stages of boiling on a heater with w = 10 mm. Boiling is initiated through individually nucleating bubbles (Fig. 6(A)i) when the surface is subjected to low heat fluxes. As heat flux is increased, these bubbles begin to coalesce laterally, resulting in larger vapor pockets departing from the surface (Fig. 6(A)ii), eventually forming even larger vapor pockets that cover a majority of the surface (Fig. 6(A)iii). With further increase in heat flux, these vapor pockets begin to coalesce and become indiscernible from one another, and a single vapor pocket (shown by blue arrows) engulfs the entire surface (Fig. 6(A)iv).

Eventually, these coalescing vapor pockets trigger a drastic decrease in heat flux accompanied by an increase in surface temperatures, marking the CHF limit (see Section 2.5). This mechanism is typical of liquid boiling on heaters with characteristic lengths significantly larger than the capillary length. On the other hand, Fig. 6(B, C) illustrate boiling on heaters with w = 2, 1, and 0.5 mm fabricated to enhance, and ultimately fully stabilize flow hydrodynamics above the surface. The widths of the surfaces are comparable to the capillary lengths ($L_c = (\sigma/\Delta\rho g)^{1/2}$) of the tested liquids ($L_{c,w}$ = 2.73 mm, $L_{c,e}$ = 1.68 mm, $L_{c,f}$ = 0.72 mm). Here, σ (N/m) is the liquid-vapor interfacial tension, $\Delta\rho$ (kg/m^3), the difference in liquid and vapor densities of the fluid, and g (=9.8 m/s^2), the acceleration due to gravity. The subscripts w, e, and f represent water, ethanol, and FC-72, respectively. We term vapor-liquid flow conditions on such heaters as *hydrodynamically enhanced conditions* (HECs). One of our research assumptions is that if the coalescence of emerging vapor columns is somehow prevented, we can expect

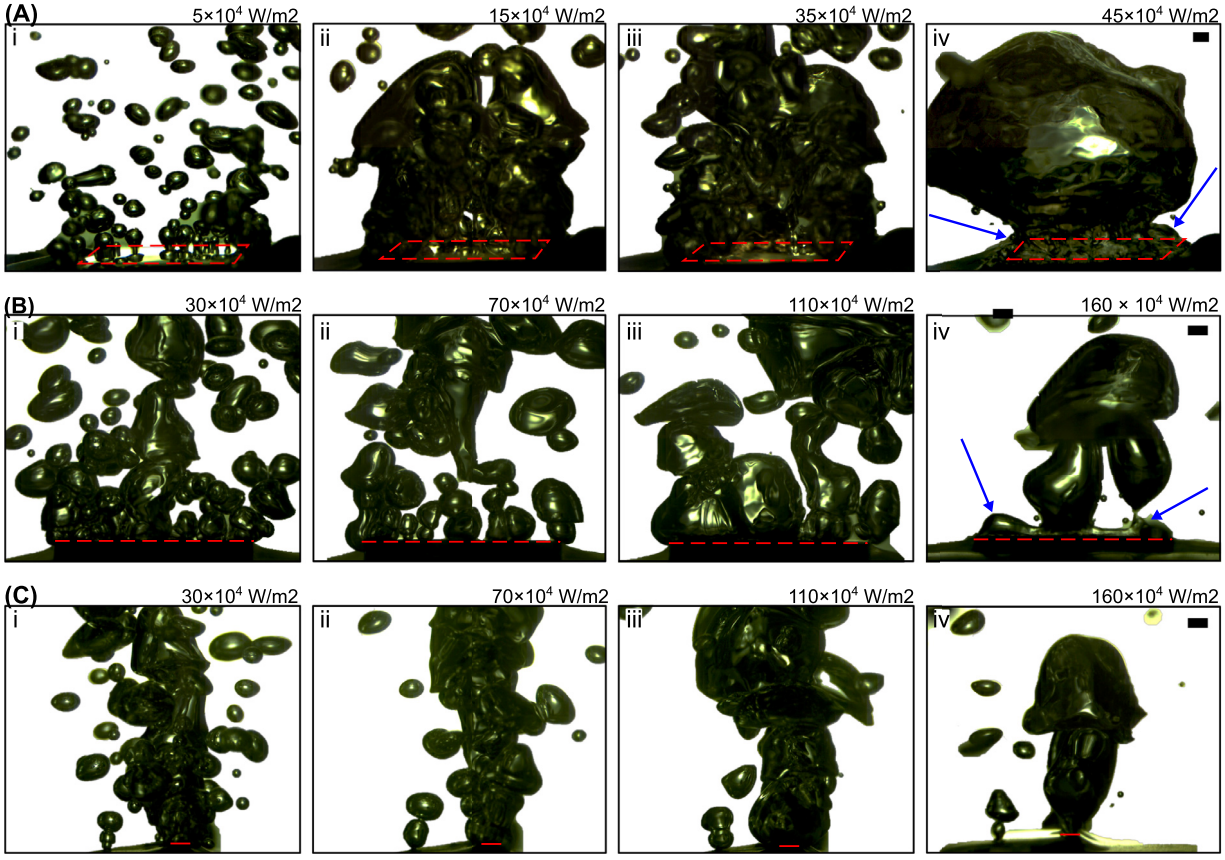

Fig. 6. Mechanistic aspects of boiling are similar for all tested liquids and the trends presented here pertain to all liquids. Images are extracted from high-speed movies captured synchronously at orthogonal angles. All images are extracted from experiments with ethanol at 101 kPa. Images in (A) are from an experiment on a heater of w = 10 mm, and images in (B) and (C) are from an experiment on a heater with w = 1 mm. Heat flux increases from left to right in the panel of images. (B) shows the longer side of heaters under hydrodynamically enhanced conditions (HECs), and (C), the shorter side of heaters under HECs. Red dashed lines help discern the heater boundaries. Boiling on heaters of w = 10 mm, shown in (A), begins with individually nucleating bubbles at low heat fluxes (i). Higher heat fluxes promote lateral bubble coalescence (ii) which results in the formation of larger vapor pockets (iii), eventually leading to CHF (iv) where a vapor blanket (shown by blue arrows) covers the entire surface. Boiling under HECs is similar to square heaters at lower heat fluxes (i, ii). However, the liquid contact line is pinned to the surface at higher heat fluxes (iii) allowing a stable vapor-liquid flow atop the surface. This flow configuration permits a much higher heat flux across the surfaces before CHF is observed (iv). Blue arrows show a vapor blanket covering the entire surface in (B)(iv). The heat flux corresponding to each image is provided on the top right corner of each image. Scale bars apply to the respective row of images, and are 1 mm.

to surpass the hydrodynamic limit. Our choice of heater widths arises from this rationale, as we expect to minimize the coalescence of vapor columns, stabilize vapor flow above the surface, and promote liquid replenishment to the surface. Here, again, it is important to note that no marked difference is observed in the mechanistic behavior of liquids across all HECs and therefore we make no distinction between the three narrow heaters. Images in Fig. 6(B, C) are extracted from an experiment run on a 1 mm wide heater, however, the mechanistic behavior shown is representative of all liquids under HECs.

Fig. 6(B) illustrates visualization of boiling on the longer (l = 10 mm) side of the heater while Fig. 6(C) represents synchronized images of the same instants in time from the narrow (w = 2, 1, 0.5 mm) side of the heaters. Boiling initiation under HECs is like square heaters where individually nucleating bubbles form the primary mechanism of heat transfer at lower heat fluxes (Fig. 6(B, C)(i)). An increase in heat flux leads to lateral coalescence of bubbles to form vapor pockets (Fig. 6(B, C)(ii, iii)); however, a distinctive feature of boiling under HECs is improved rewetting along the length (l) of the heater. This replenishment of liquid is possible since coalescence of vapor columns is now primarily restricted to one direction along the heater length. At higher heat fluxes, vapor pockets grow but are eventually constrained at the heater boundary to form a stable vapor pathway comparable to a single vapor column rising above the surface. This liquid pinning facilitates rewetting along the heater length otherwise hindered by multiple interacting vapor columns. At these HECs, the sustained vapor-liquid flow hydrodynamic allows for a heat flux well beyond Zuber's limit. Further increase in heat flux rapidly expands the contact line, covering the entire heater surface and extending onto the surrounding area (depicted by blue arrows), and CHF is observed. The recorded CHF values on all heaters at various pressures are plotted in Fig. 7(A–C)..

An initial observation shows CHF values decreasing with a reduction in saturation pressure consistent with previous reports of boiling under reduced pressures [42]. However, a more important result is a steady increase in CHF values as the heater width is reduced. Since the square heater has a characteristic length greater than the capillary length of all liquids, CHF is limited by hydrodynamic instabilities, evidenced by the pink curves depicting Zuber's correlation [32], as given in Eq. (3)

$$CHF_{Zuber} = \frac{\pi}{24} h_{fg} \rho_v^{1/2} [\sigma g(\rho_l - \rho_v)]^{1/4} \quad (3)$$

which considers the interaction of vapor columns away from the surface and does not account for the contact angle of the liquid. As the characteristic length of the heaters is gradually decreased closer to the liquid capillary length, CHF progressively increases. This trend is brought about by stabilization of the liquid-vapor hydrodynamics above the surface which is most evident in the case of water (Fig. 7(A)) where heaters with w = 2 mm, 1 mm, and

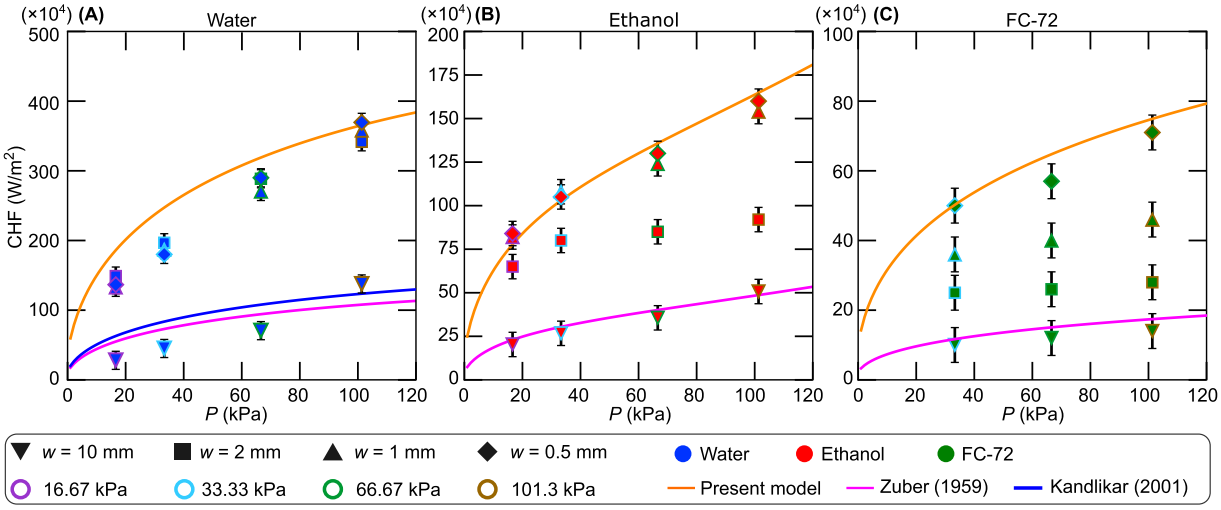

Fig. 7. Critical heat flux (CHF) on different surfaces for (A) water, (B) ethanol, and (C) FC-72. Inverted triangles represent surfaces with a width of 10 mm; squares, 2 mm; upright triangles, 1 mm; and diamonds, 0.5 mm. The error bars represent the uncertainty in recording the heat fluxes. The pink curves represent Zuber's prediction [32] for the respective liquid and surface configuration, orange curves represent the present model (see Section 3.2), while the blue curve represents Kandlikar's prediction [36].

0.5 mm are smaller than water's capillary length ($L_{c,w}$ = 2.73 mm). Under fully stabilized flow hydrodynamics, CHF values for water markedly exceed Zuber's hydrodynamic limit, reaching their highest at atmospheric pressure with a value close to four times that of Zuber's limit. Considering the case of ethanol (Fig. 7(B)), the CHF limit increases to some degree on a 2 mm wide heater compared to the square heater due to enhanced hydrodynamic stability; however, further decrease in heater width below the liquid capillary length fully stabilizes flow hydrodynamics resulting in further rise in the CHF limit. This progressively increasing trend is most recognizable in the case of FC-72 (Fig. 7(C)) wherein gradual stabilization of vapor-liquid flow hydrodynamics results in steady increase in CHF, reaching an ultimate value on a heater whose width (w = 0.5 mm) is lower than FC-72's capillary length (L_{cf} = 0.72 mm). A balance between the evaporation momentum and the restoring surface tension forces closely predicts CHF limits under fully stabilized conditions and is represented by the orange lines in Fig. 7 (see Section 3.2 for details on the model). The above trends indicate stabilization of flow hydrodynamics through modification of the heaters geometries, resulting in the evaporation momentum force becomeing the limiting mechanism, albeit, at a much higher value than previously estimated [36].

Secondly, while CHF limits dramatically increase as heater size is reduced below the liquid capillary length, a further decrease in width does not enhance CHF. This phenomenon is most apparent in the case of water (Fig. 7(A)) where CHF values plateau at their unique values even as the heater width is decreased to 0.5 mm, roughly 5 times lower than its capillary length of 2.73 mm. A similar upper bound on the heat flux values is observed in the case of ethanol (see Fig. 7(B)) where the CHF values do not increase when the heater width is reduced from 1 mm to 0.5 mm. This suggests an ultimate limit for heat transfer from planar surfaces. These results suggest that the evaporation momentum force is present throughout the boiling process; however, hydrodynamics of fluid flow on large heaters prematurely inhibits surface rewetting, leading to CHF at heat fluxes inferior to the evaporation momentum limit. Our results are also in contrast to a recent study [43] which used 84 experimental CHF data points in a neural network model to conclude that "CHF maximization is dominantly affected by far field fluid properties and is maximized when heater size is ~8 mm". This could be a result of the dataset chosen by the authors which includes only square heaters with a minimum size of 8 mm.

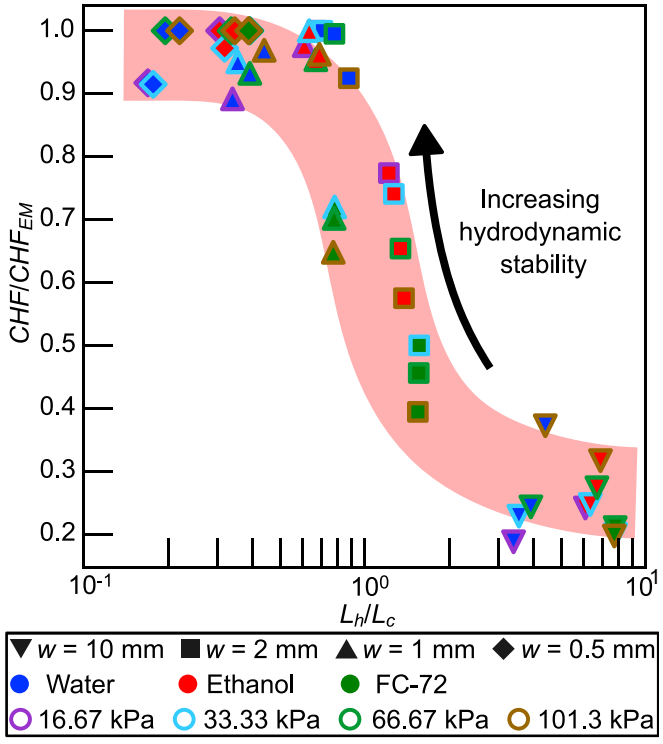

Fig. 8. The CHF obtained in all test cases is normalized using the maximum measured CHF of the specific liquid at the corresponding pressure and is plotted as a function of the characteristic length ($L_h = w$) non-dimensionalized using the capillary length of the liquid (L_c). Marker shapes represent different surfaces, face colors represent liquids, and the edge colors represent the experimental pressures.

The foregoing results lead to important insights regarding the limits of heat transfer from a surface to the surrounding fluid. Most importantly, we find that the capillary length plays a vital role in determining the limiting mechanism of the pool boiling crisis. The CHF measured in our experiments is normalized using the measured evaporation momentum limit (CHF_{EM}) of the corresponding liquid at the corresponding pressure and is plotted (Fig. 8) as a function of the characteristic heater length (in this case, the heater width; $L_h = w$) non-dimensionalized using the liquid cap-

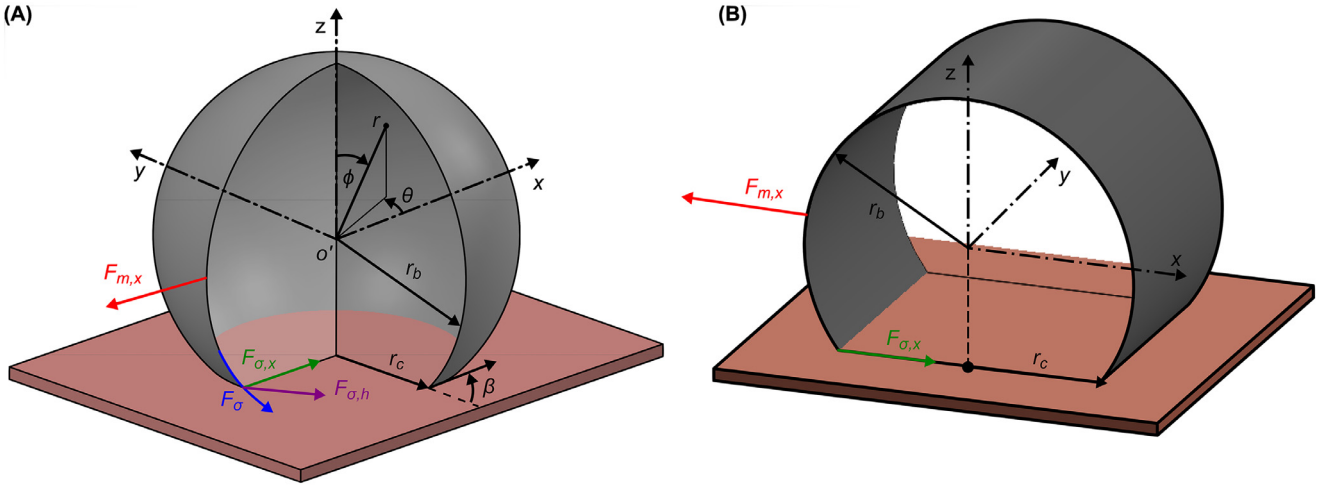

Fig. 9. (A) Geometry and forces considered in deriving the CHF limit based on evaporation momentum theory. $F_{m,x}$ represents the component of the evaporation momentum force acting in the x-direction, F_σ represents the interfacial tension force, $F_{\sigma,h}$ represents the component of interfacial tension force acting on the horizontal x-y plane, and $F_{\sigma,x}$ represents the component of the interfacial tension force acting in the x-direction on the x-y plane. β is the liquid contact angle, θ is the azimuthal angle, and ϕ is the polar angle in the spherical coordinates. r_b is the radius of the spherical cap and r_c is the radius of contact of the bubble with the surface. (B) Force balance considered by Kandlikar [36].

illary length (L_c). This ratio can also be expressed as the square root of the Bond number (such that $(L_h/L_c)^2 = Bo = (\rho g L_h^2)/\sigma$) which quantifies the relative importance between the gravitational and capillary forces. Fig. 8 enunciates that progressively stabilizing flow hydrodynamics through a reduction in heater dimensions enhances CHF beyond Zuber's limit. CHF is ultimately limited by the evaporation momentum limit as flow is fully stabilized on heaters smaller than the capillary lengths of the liquid. This trend is consistent across all test cases, independent of the liquid, heater size, and pressure.

3.2. Theoretical interpretation

To predict CHF values when liquid flow is hydrodynamically stable on top of the surface, we examine the evaporation momentum theory. We begin by considering a single vapor pocket on a horizontal surface as shown in Fig. 9(A). The vapor pocket can be idealized to a spherical cap to simplify numerical analysis. This contrasts with the cylindrical geometry assumption by Kandlikar [36] shown in Fig. 9(B). The bubble constitutes of vapor with density ρ_v surrounded by a liquid with density ρ_l, and a radius r_b. The radius of contact with the surface is denoted by r_c, σ denotes interfacial tension between the liquid and vapor, β denotes liquid contact angle, and g is the acceleration due to gravity. The origin O' is at the geometric center of the sphere supporting the bubble and any point on the sphere can be mapped using the radial (r), azimuthal (θ), and polar ($\emptyset$) coordinates in the spherical coordinate system, while x, y, z represent the cartesian axes as shown in Fig. 9(A).

The evaporation momentum force F_m acts to expand the vapor pocket radially outward, while the surface tension force F_σ (shown by the blue arrow) constrains this expansion. An additional buoyancy force also acts on the interface of the bubble, but primarily in the vertical direction and hence does not contribute to the lateral expansion of the pocket. To estimate the condition for CHF, we balance the horizontal components of the two forces, specifically in the x-direction. The analysis is performed on the left half of the bubble, and hence the net evaporation momentum force $F_{m,x}$ acts along the negative x-axis unlike shown in Fig. 9(A) for clarity. First, we evaluate the x-component of the evaporation momentum force acting on left half of the vapor pocket $F_{m,x} = \int V_x \rho_v (\vec{V} \cdot \vec{n}) d\boldsymbol{A}$, where V_x is the component of vapor velocity in the x-direction, $\vec{V} \cdot \vec{n}$ is the magnitude of vapor velocity in the direction normal to the pocket's interface, and $d\boldsymbol{A} = r_b^2 \sin\emptyset \cdot d\theta \cdot d\emptyset$ is the differential area element of a sphere.

The mass flux of evaporating vapor is given by $\dot{m} = q'' A_i / h_{fg}$, where q'' is the incident heat flux contributing to the vapor generation, A_i $(= 4\pi r_b^2)$ is the area of influence responsible for supplying heat to the bubble, and h_{fg} is the latent heat of vaporization of the liquid. The mass flux can also be expressed as $\dot{m} = \rho_v A_b v$, where A_b is the surface area of the bubble/vapor pocket, and hence we can express the velocity of the vapor at the liquid-vapor interface $v = 4q''/(\rho_v h_{fg}(1+\cos\beta))$. The x-component of the velocity $v_x = v \cdot r\cos\theta \sin\emptyset$, hence, the horizontal x-component of the evaporation momentum force acting on the left half of the spherical cap is given by Eq. (4).

$$F_{m,x} = \left(\frac{q''}{h_{fg}}\right)^2 \frac{4r_b^2}{\rho_v (1+\cos\beta)^2}\left[(\pi-\beta) + \frac{1}{2}\sin 2\beta\right] \tag{4}$$

Next, the horizontal component of the surface tension force acting in the x-direction is evaluated. Considering the surface tension force as shown in Fig. 9(A), we see that F_σ (shown by the blue arrow) acts along the interface of the vapor pocket. $F_\sigma = \int dF_\sigma$, where $dF_\sigma (= \sigma \cdot dl)$ is the differential surface tension force and $dl (= r_b \cdot d\theta)$ is the differential line element on the liquid-vapor interface. Resolving this force into horizontal and vertical components, the horizontal component is given by $F_{\sigma,h} = F_\sigma \cos\beta$ (depicted by the purple arrow). The component of $F_{\sigma,h}$ in the x-direction is given by $F_{\sigma,x} = F_{\sigma,h}\cos\theta$. Similarly, the surface tension acting on the free surface of the left half of the bubble in the y-z plane can be estimated by integrating the differential surface tension element $(\sigma r_b d\alpha)$ over the contour of the sphere in the y-z plane where α is the angle made by the differential element with the positive z axis and varies from $-(\pi-\beta)$ to $(\pi-\beta)$. The total surface tension force opposing the evaporation momentum force can accordingly be written as given in Eq. (5).

$$F_{\sigma,x} = 2\sigma r_b(\pi - \beta + \cos\beta) \tag{5}$$

CHF is triggered when the surface tension force is equal to the evaporation momentum force, and hence balancing

Eqs. (4) and (5) yields the expression for critical heat flux as given in Eq. (6).

$$CHF_{EM} = h_{fg}\rho_v^{1/2}[\sigma g(\rho_l - \rho_v)]^{1/4}\left\{\frac{(1+\cos\beta)}{[3\pi^2]^{1/4}}\left[\frac{\pi - \beta + \cos\beta}{\pi - \beta + \frac{\sin 2\beta}{2}}\right]^{1/2}\right\} \quad (6)$$

where the bubble diameter ($d_b = 2r_b$) is expressed as half the critical wavelength of Taylor instability, $d_b = \sqrt{3}\pi[\sigma/\Delta\rho g]^{1/2}$[32]. Here, $\Delta\rho(=\rho_l - \rho_v)$ is the difference in liquid and vapor densities of the fluid. Thermo-fluid properties for the tested liquids obtained from REFPROP, a Standard Reference Database distributed by the National Institute of Standards and Technology (NIST) [44] and dynamic contact angles of 60° for water, 45° for ethanol, and 20° for FC-72, extracted from experimental images, were used in Eq. (6) to estimate the theoretical CHF limit. The orange line in Fig. 8 represents Eq. (6) and closely matches all experimental data. The current prediction is plotted alongside the theoretical model proposed by Kandlikar [36] (Eq. (7)) in Fig. 7 since the fundamental physics considered in the two models is the same.

$$CHF_{Kandlikar} = h_{fg}\rho_v^{1/2}[\sigma g(\rho_l - \rho_v)]^{1/4}\left(\frac{1+\cos\beta}{16}\right) \times\left\{\frac{2}{\pi} + \frac{\pi}{4}(1+\cos\beta)\cos\emptyset\right\} \quad (7)$$

Here, $\emptyset$ is the angle of inclination of the surface with the horizontal ($\emptyset = 0$ for a horizontal surface). Our experimental and theoretical analysis indicate that the evaporation momentum limit is fundamentally different from the hydrodynamic limit, in contrast to previous studies where the physics of evaporation momentum has been utilized to explain CHF on large surfaces. We suppose that the geometric considerations in previous estimates of the evaporation momentum limit, namely that of an infinitely long cylinder resting on the heater surface, result in CHF predictions close to the hydrodynamic limit.

4. Conclusion

We studied pool boiling of 3 different liquids; namely water, ethanol, and FC-72 with vastly different properties to greatly vary the capillary length (L_c). In addition, tests were conducted at different saturation pressures (corresponding to different saturation temperatures) to further widen the range of L_c. We varied heater widths (w, or L_h) from an order of magnitude above L_c to below L_c such that 48 unique CHF values were probed spanning over an order of magnitude of L_h/L_c. As L_h/L_c is reduced, hydrodynamics of the flow progressively stabilizes, leading to a steady increase in CHF. As L_h/L_c approaches 1, CHF rapidly increases and when L_h/L_c is reduced below ~1, surface experiences CHF_{EM}. In other words, CHF_{EM} limit is observed for $L_h/L_c < 1$ and hydrodynamic limit for $L_h/L_c > 1$. For water, with a L_c of 2.73 mm at 1 atm, the 2-,1-, and 0.5-mm wide strip heaters experience CHF_{EM}. In the case of ethanol (with L_c of 1.6 mm at 1 atm), a 2-mm-wide surface was limited hydrodynamically, whereas 1-, and 0.5-mm-wide heaters experienced CHF_{EM}. FC-72 on the other hand (with L_c of 0.72 mm at 1 atm) experienced CHF_{EM} only on the 0.5-mm-wide heater, not on the 1-mm-wide heater. Normalized CHF i.e., CHF/CHF_{EM} plotted versus L_h/L_c shows a universal trend wherein CHF/CHF_{EM} continuously rises as L_h/L_c decreases and rapidly surges at $L_h/L_c \sim 1$, unambiguously delineating the deterministic character of L_c in deciding whether CHF is limited hydrodynamically or not. Finally, we modeled CHF_{EM} using a force balance on a bubble and find that the consideration of a spherical geometry is requisite for its correct estimation.

Declaration of Competing Interest

The authors declare that they have no known competing financial interests or personal relationships that could have appeared to influence the work reported in this paper.

CRediT authorship contribution statement

Suhas Tamvada: Methodology, Software, Formal analysis, Investigation, Data curation, Writing – original draft, Writing – review & editing, Visualization. **Daniel Attinger:** Validation, Formal analysis, Writing – review & editing. **Saeed Moghaddam:** Conceptualization, Methodology, Validation, Formal analysis, Resources, Writing – review & editing, Supervision, Project administration, Funding acquisition.

Data availability

Data will be made available on request.

Acknowledgments

This work is supported by Award No. CBET 1934354 from the United States National Science Foundation (NSF).

Supplementary materials

Supplementary material associated with this article can be found, in the online version, at doi:10.1016/j.ijheatmasstransfer.2022.123837.

References

[1] R. Chen, M.C. Lu, V. Srinivasan, Z. Wang, H.H. Cho, A. Majumdar, Nanowires for enhanced boiling heat transfer, Nano Lett. 9 (2009) 548–553, doi:10.1021/nl8026857.
[2] S. Kalogirou, Survey of solar desalination systems and system selection, Energy 22 (1997) 69–81, doi:10.1016/S0360-5442(96)00100-4.
[3] T. Liu, M.S. Mauter, Heat transfer innovations and their application in thermal desalination processes, Joule 6 (2022) 1199–1229, doi:10.1016/J.JOULE.2022.05.004.
[4] A. Bejan, A.D. Kraus, Heat Transfer Handbook, John Wiley & Sons, 2003.
[5] H. Lv, H. Ma, N. Mao, T. He, Boiling heat transfer mechanism of environmental-friendly refrigerants: a review, Int. J. Refrig. 133 (2022) 214–225, doi:10.1016/J.IJREFRIG.2021.10.007.
[6] R. Wen, X. Ma, Y.C. Lee, R. Yang, Liquid-vapor phase-change heat transfer on functionalized nanowired surfaces and beyond, Joule 2 (2018) 2307–2347, doi:10.1016/J.JOULE.2018.08.014.
[7] V.P. Carey, Liquid-Vapor Phase-Change Phenomena, CRC Press, 2020, doi:10.1201/9780429082221.
[8] Todreas, N.E., & Kazimi, M.S. (2021). Nuclear Systems Volume I: Thermal Hydraulic Fundamentals, Third Edition (3rd ed.). CRC Press. doi:10.1201/9781351030502.
[9] S. NUKIYAMA, The Maximum and minimum values of the heat Q transmitted from metal to boiling water under atmospheric pressure, J. Soc. Mech. Eng. 37 (1934) 367–374, doi:10.1299/jsmemagazine.37.206_367.
[10] A.B. Ponter, C.P. Haigh, The boiling crisis in saturated and subcooled pool boiling at reduced pressures, Int. J. Heat Mass Transf. 12 (1969) 429–437, doi:10.1016/0017-9310(69)90138-0.
[11] W.R. McGillis, V.P. Carey, J.S. Fitch, W.R. Hamburgen, Pool boiling enhancement techniques for water at low pressure, in: Proceedings of the 7th IEEE Semiconductor Thermal Measurement and Management Symposium, IEEE, 1991, pp. 64–72, doi:10.1109/STHERM.1991.152914.
[12] J.H. Lienhard, V.E. Schrock, The effect of pressure, geometry, and the equation of state upon the peak and minimum boiling heat flux, J. Heat Transf. 85 (1963) 261–268, doi:10.1115/1.3686092.
[13] B. Shen, T. Hamazaki, W. Ma, N. Iwata, S. Hidaka, A. Takahara, K. Takahashi, Y. Takata, Enhanced pool boiling of ethanol on wettability-patterned surfaces, Appl. Therm. Eng. 149 (2019) 325–331, doi:10.1016/j.applthermaleng.2018.12.049.
[14] C.H. Wang, V.K. Dhir, Effect of surface wettability on active nucleation site density during pool boiling of water on a vertical surface, J. Heat Transf. 115 (1993) 659–669, doi:10.1115/1.2910737.
[15] S.J. Kim, I.C. Bang, J. Buongiorno, L.W. Hu, Surface wettability change during pool boiling of nanofluids and its effect on critical heat flux, Int. J. Heat Mass Transf. 50 (2007) 4105–4116, doi:10.1016/j.ijheatmasstransfer.2007.02.002.

[16] M.M. Rahman, E. Ölçeroğlu, M. McCarthy, Role of wickability on the critical heat flux of structured superhydrophilic surfaces, Langmuir 30 (2014) 11225–11234, doi:10.1021/la5030923.
[17] H. Hu, J.A. Weibel, S.v. Garimella, A coupled wicking and evaporation model for prediction of pool boiling critical heat flux on structured surfaces, Int. J. Heat Mass Transf. 136 (2019) 373–382, doi:10.1016/j.ijheatmasstransfer.2019.03.005.
[18] A. Fazeli, S. Moghaddam, A new paradigm for understanding and enhancing the critical heat flux (CHF) limit, Sci Rep. 7 (2017) 5184, doi:10.1038/s41598-017-05036-2.
[19] M. Alipanah, S. Moghaddam, Ultra-low pressure drop membrane-based heat sink with 1000W/cm^2 cooling capacity and 100% exit vapor quality, Int. J. Heat Mass Transf. 161 (2020) 120312, doi:10.1016/j.ijheatmasstransfer.2020.120312.
[20] S.R. Tamvada, M. Alipanah, S. Moghaddam, Membrane-based two phase heat sinks for high heat flux electronics and lasers, IEEE Trans. Compon. Packag. Manuf. Technol. 11 (2021) 1734–1741, doi:10.1109/TCPMT.2021.3115419.
[21] B.J. Jones, J.P. McHale, S.v. Garimella, The influence of surface roughness on nucleate pool boiling heat transfer, J. Heat Transf. 131 (2009) 1–14, doi:10.1115/1.3220144/415333.
[22] H. O'Hanley, C. Coyle, J. Buongiorno, T. McKrell, L.W. Hu, M. Rubner, R. Cohen, Separate effects of surface roughness, wettability, and porosity on the boiling critical heat flux, Appl. Phys. Lett. 103 (2013) 024102, doi:10.1063/1.4813450.
[23] J. Kim, S. Jun, R. Laksnarain, S.M. You, Effect of surface roughness on pool boiling heat transfer at a heated surface having moderate wettability, Int. J. Heat Mass Transf. 101 (2016) 992–1002, doi:10.1016/J.IJHEATMASSTRANSFER.2016.05.067.
[24] J.H. Lienhard, V.K. Dhir, Hydrodynamic prediction of peak pool-boiling heat fluxes from finite bodies, J. Heat Transf. 95 (1973) 152–158, doi:10.1115/1.3450013.
[25] J.H. Lienhard, V.K. Dhir, D.M. Riherd, Peak pool boiling heat-flux measurements on finite horizontal flat plates, J. Heat Transf. 95 (1973) 477–482, doi:10.1115/1.3450092.
[26] J.H. Lienhard, K. Watanabe, On correlating the peak and minimum boiling heat fluxes with pressure and heater configuration, J. Heat Transf. 88 (1966) 94–99, doi:10.1115/1.3691491.
[27] S.M. Kwark, M. Amaya, R. Kumar, G. Moreno, S.M. You, Effects of pressure, orientation, and heater size on pool boiling of water with nanocoated heaters, Int. J. Heat Mass Transf. 53 (2010) 5199–5208, doi:10.1016/j.ijheatmasstransfer.2010.07.040.
[28] K.N. Rainey, S.M. You, Effects of heater size and orientation on pool boiling heat transfer from microporous coated surfaces, Int. J. Heat Mass Transf. 44 (2001) 2589–2599, doi:10.1016/S0017-9310(00)00318-5.
[29] R. Raj, J. Kim, Heater size and gravity based pool boiling regime map: transition criteria between buoyancy and surface tension dominated boiling, J. Heat Transf. 132 (2010) 1–10, doi:10.1115/1.4001635.
[30] I.I. Gogonin, S.S. Kutateladze, Critical heat flux as a function of heater size for a liquid boiling in a large enclosure, J. Eng. Phys. 33 (1977) 1286–1289, doi:10.1007/BF00860899.
[31] S.S. Kutateladze, On the transition to film boiling under natural convection, Kotloturbostroenie 3 (1948) 20 https://cir.nii.ac.jp/crid/1571698601178449536. (accessed July 23, 2022).
[32] N. Zuber, Hydrodynamic Aspects Of Boiling Heat Transfer, Oak Ridge, TN, 1959 (Thesis), doi:10.2172/4175511.
[33] Lienhard„ J.H. and Witte„ L.C. "An Historical Review of the Hydrodynamic Theory of Boiling" *Reviews in Chemical Engineering*, vol. 3, no. 3-4, 1985, pp. 187-280. doi:10.1515/REVCE.1985.3.3-4.187
[34] Y. Haramura, Y. Katto, A new hydrodynamic model of critical heat flux, applicable widely to both pool and forced convection boiling on submerged bodies in saturated liquids, Int. J. Heat Mass Transf. 26 (1983) 389–399, doi:10.1016/0017-9310(83)90043-1.
[35] A. Steinchen, K. Sefiane, Stability analysis of the pool-boiling crisis, J. Phys. Condens. Matter 8 (1996) 9565, doi:10.1088/0953-8984/8/47/063.
[36] S.G. Kandlikar, A theoretical model to predict pool boiling CHF incorporating effects of contact angle and orientation, J. Heat Transf. 123 (2001) 1071–1079, doi:10.1115/1.1409265.
[37] G.I. Taylor, The instability of liquid surfaces when accelerated in a direction perpendicular to their planes. I, Proc. R. Soc. Lond. A Math. Phys. Sci. 201 (1950) 192–196, doi:10.1098/rspa.1950.0052.
[38] Professor Helmholtz (1868) XLIII. *On discontinuous movements of fluids*, The London, Edinburgh, and Dublin Philosophical Magazine and Journal of Science, 36:244, 337-346, doi:10.1080/14786446808640073.
[39] J. Reed and V. K. Dhir, "Assessment of Critical Heat Flux on Finite Size Surfaces Under Pool Boiling," 2019 35th Semiconductor Thermal Measurement, Modeling and Management Symposium (SEMI-THERM), 2019, pp. 18-25.
[40] V.v. Yagov, Is a crisis in pool boiling actually a hydrodynamic phenomenon? Int. J. Heat Mass Transf. 73 (2014) 265–273, doi:10.1016/j.ijheatmasstransfer.2014.01.076.
[41] M.M. Rahman, J. Pollack, M. McCarthy, Increasing boiling heat transfer using low conductivity materials, Sci. Rep. 5 (2015) 13145, doi:10.1038/srep13145.
[42] A. Surtaev, V. Serdyukov, I. Malakhov, Effect of subatmospheric pressures on heat transfer, vapor bubbles and dry spots evolution during water boiling, Exp. Therm Fluid Sci. 112 (2020) 109974, doi:10.1016/j.expthermflusci.2019.109974.
[43] M. He, Y. Lee, Revisiting heater size sensitive pool boiling critical heat flux using neural network modeling: heater length of the half of the Rayleigh-Taylor Instability Wavelength maximizes CHF, Therm. Sci. Eng. Prog. 14 (2019), doi:10.1016/j.tsep.2019.100421.
[44] E.W. Lemmon, I.H. Bell, M.L. Huber, M.O. McLinden, NIST Standard Reference Database 23: Reference Fluid Thermodynamic and Transport Properties-REFPROP, Version 10.0, National Institute of Standards and Technology, 2018, doi:10.18434/T4/1502528.